R. Prakash Kolli[a], David N. Seidman[a,b]
[a] Department of Materials Science and Engineering, Northwestern University, Evanston, Illinois, USA
[b] Northwestern University Center for Atom-Probe Tomography (NUCAPT), Evanston, Illinois, USA

Coarsening kinetics of Cu-rich precipitates in a concentrated multicomponent Fe–Cu based steel

Dedicated to Prof. Dr.-Ing. Heinrich Wollenberger on the occasion of his 80th birthday

The coarsening kinetics of Cu-rich precipitates in a concentrated multicomponent Fe–Cu based steel, containing 1.12 at.% Cu, aged at 550 °C or at 550 °C plus 2 h at 200 °C is investigated. The temporal evolution of the precipitates, heterophase interfaces, and α-Fe matrix compositions and precipitate morphology are presented. Coarsening time exponents are determined for the mean radius, $\langle R(t)\rangle$, and number density, $N_V(t)$, and compared to the Lifshitz–Slyzov–Wagner model for coarsening, modified for concentrated multicomponent alloys by Umantsev–Olson. The experimental results indicate that $\langle R(t)\rangle$ and $N_V(t)$ are in reasonable agreement with Umantsev–Olson model behavior. Additionally, we compare the results to earlier investigations of similar concentrated multicomponent steels containing 1.82 at.% Cu and 1.17 at.% Cu, aged at 500 °C.

Keywords: Coarsening; Phase separation; Fe–Cu alloys; Atom-probe tomography; Precipitation

1. Introduction

Copper precipitation-strengthened steels are of considerable commercial importance due to their high strength, good impact toughness, excellent weldability without preheat or postheat, and corrosion resistance [1–4]. This desirable combination of properties is derived from Cu precipitates, formed after solutionizing in the γ-phase (fcc) field and thermal aging below the eutectoid transformation temperature, found within these steels. The phase decomposition of binary, ternary, and quaternary Fe–Cu based carbon-free alloys or low-carbon steels has been studied utilizing Mössbauer spectroscopy [5], field-ion microscopy (FIM) [6, 7], atom-probe field-ion microscopy (APFIM) [8–11], atom-probe tomography (APT) [12], conventional and high-resolution electron microscopies (CTEM and HREM) [11, 13–20], small-angle neutron scattering (SANS) [21–24], extended X-ray absorption fine structure (EXAFS) [25], X-ray absorption spectroscopy (XAS) [26], small-angle X-ray scattering (SAXS) [13, 19], and computer simulations [27–34]. Fewer studies exist on multicomponent steels with increasing alloying content and microstructural complexity. The recent studies of Vaynman et al. [2] and Isheim et al. [35–37] characterized the Cu-rich precipitates found within multicomponent F–Cu based steels at near-peak microhardness and in the slightly overaged condition.

We have recently reported on the phase decomposition of similar concentrated multicomponent F–Cu based steels containing 1.82 at.% Cu, denoted NUCu-170 (170 designates the yield strength in ksi) [38], and 1.17 at.% Cu, denoted NUCu-140-1 (140 is the yield strength and 1 designates the experimental heat number) [39]. We described in detail the temporal evolution of the morphology and composition of the Cu-rich precipitates from the as-quenched condition to 1 024 h, when aged at 500 °C. The results were compared to the Lifshitz–Slyzov–Wagner (LSW) model [40, 41] for coarsening, modified for concentrated multicomponent alloys by Umantsev and Olson (UO) [42], and shown *not* to satisfy strictly the temporal dependencies for mean radius, $\langle R(t)\rangle$; number density, $N_V(t)$; and matrix (mat.), precipitate (ppt.), and interface (int.) supersaturations, $\Delta C_i^j(t)$, of an element i in phase j (j = mat., ppt., and int.). The temporal dependency for $\langle R(t)\rangle$ agrees with the 1/3 model prediction only at aging times greater than 64 h, whereas the exponent for $N_V(t)$ is less than the -1 model prediction, even to an aging time of 1 024 h. The differences between the experimentally determined results and the UO model predictions are due to violations of the assumptions of the model, which affect the growth and coarsening behavior of the precipitates. The morphology of the precipitates becomes rod-like at longer aging times because of elastic strain-energy effects, the composition of the Cu-rich precipitates evolve temporally, an $Ni_{0.5}(Al_{0.5-x}Mn_x)$ phase forms at the heterophase interfacial region [43], the precipitates are known to change phase, and the system has not achieved a stationary state. Earlier investigations on the growth and coarsening of binary Fe–Cu carbon-free alloys at aging temperatures between 600 and 830 °C, which is greater than the 500 °C we employed, reported good agreement with the $t^{1/3}$ power-law for $\langle R(t)\rangle$ [15, 44, 45].

The focus of this investigation is the coarsening of the Cu-rich precipitates in a concentrated multicomponent Fe–Cu based steel containing 1.12 at.% Cu. This steel is being studied as part of a program to develop an explosion resistant steel for the US Navy [2, 46, 47]. This steel, denoted NUCu-140-3, has the same nominal composition as the NUCu-140-1 steel in Ref. [39] but is aged at 550 °C rather than 500 °C. The steels, when aged at 550 °C, attain better Charpy V-notch (CVN) absorbed impact-energy values when compared to aging at 500 °C; aging at 500 °C, however, results in higher yield-strengths [2]. In this article we present results on the temporal evolution of the morphology and compositions of the Cu-rich precipitates from 0.25 to

4 h, when aged at 550 °C and also for the same times at 550 °C plus 2 h at 200 °C (double-aging treatment), utilizing atom-probe tomography (APT). The power-law time exponents are experimentally determined for $\langle R(t)\rangle$ and $N_V(t)$. The results are discussed in context of the UO model and compared to the results of the NUCu-170 [38] and the NUCu-140-1 [39] steels.

2. Experimental methods

2.1. Material details

A 45.5 kg (100 lb) steel heat was vacuum induction melted and cast at ArcelorMittal Steel Global Research & Development, East Chicago, Indiana. The heat was reheated to approximately 1 150 °C and hot-rolled in multiple passes to a thickness of 12.5 mm and air-cooled to room temperature. The final hot-rolling temperature was 900 °C. The bulk composition of the steel (NUCu-140-3), determined by spectrographic analysis at ArcelorMittal Steel Global Research & Development, is presented in Table 1. The plates were trimmed and cut into rods 12.5 mm × 12.5 mm × 250 mm and solutionized at 900 °C for 1 h and then quenched into water at 25 °C. Specimens (12.5 mm × 12.5 mm × 25 mm blocks) for microhardness testing and APT were aged at 550 °C for 0.25, 1, or 4 h and subsequently quenched into water at 25 °C. A second group of specimens received the same thermal treatment and were then additionally aged for 2 h at 200 °C and subsequently quenched into water at 25 °C (double-aging treatment).

2.2. Vickers microhardness

Sections were cold mounted in acrylic and polished utilizing standard metallographic procedures to a final surface finish of 1 μm for microhardness testing. Microhardness testing was performed in accordance with ASTM standards (ASTM E 384-99) using a Buehler Micromet II microhardness tester with a Vickers microhardness indenter, a load of 500 g, and a testing time of 15 s. The reported microhardness values are derived from 10 measurements on each specimen.

2.3. Atom-probe tomography

The steel blocks were further reduced to 0.3 mm × 12.5 mm × 25 mm coupons, which were cut from the center utilizing an abrasive saw. The APT tip blanks (0.3 mm × 0.3 mm × 25 mm) were mechanically cut from the coupons and electropolished using standard techniques [48, 49]. Initial polishing was performed with a solution of 10 vol.% perchloric acid in acetic acid at 15–10 Vdc at room temperature. This was followed by a manually controlled pulsed final-polishing procedure using a solution of 2 vol.% perchloric acid in butoxyethanol at 10–5 Vdc at room temperature, producing a tip with a radius <50 nm. Local-electrode atom-probe (LEAP) tomography employing the LEAP 3000X (Cameca (formerly Imago Scientific Instruments, Madison, WI)) [50, 51] was performed at a specimen temperature of 50 K under ultrahigh vacuum (UHV) conditions of ca. 1×10^{-8} Pa (ca. 7.5×10^{-11} torr). The pulse repetition rate was 2×10^5 Hz and the pulse-voltage-to-standing-dc voltage ratio (pulse fraction) was 15–20 %.

Visualization and reconstruction of the atom-probe data is performed using the Cameca Visualization and Analysis Software (IVAS 3.0) package. The precipitates are identified utilizing an isoconcentration surface methodology [52] with the threshold concentration set at 10 at.% Cu, which yields morphologically and compositionally stable results. The parameters chosen for obtaining noise-free isoconcentration surfaces are a voxel size of 1 nm, a delocalization distance of 4 nm, a sample count threshold of 5 %, and a polygon filter level of 10–20.

Concentration profiles with respect to distance from the reference isoconcentration surfaces are obtained utilizing the proximity histogram (proxigram for short) with a bin width of 0.25 nm [53]. The $\pm 2\sigma$ error bars for the reported concentrations are given by counting statistics,

$$\sigma = \sqrt{\frac{c_i(1-c_i)}{N_{TOT}}} \tag{1}$$

where c_i is the atomic fraction of an element i in a bin and N_{TOT} is the total number of ions in a bin.

The spherical volume equivalent radius, R, of a precipitate [54] is given by,

$$R = \left(\frac{3}{4\pi}\frac{N_{atoms}}{\rho_{th}\eta}\right) \tag{2}$$

where N_{atoms} is the number of atoms detected within a delineated precipitate; ρ_{th} is the theoretical atomic density, which is equal to 84.3 atoms nm^{-3} for this steel; and η is the estimated detection efficiency of 0.5 of the multichannel plate detector. The value of N_{atoms} belonging to a precipitate is determined from the envelope method [49, 55], based on a maximum separation distance, d_{max}, of 0.5–0.6 nm, a minimum number of solute atoms, N_{min}, of 10–100 Cu atoms (depending on the aging time), and a grid spacing of 0.2 nm. The details regarding selection of values for the parameters utilized in the envelope method for this steel are found in Ref. [54].

3. Results

3.1. Temporal evolution of the microhardness and morphology

Figure 1 displays the Vickers microhardness (VHN) as function of aging time. This figure demonstrates that an in-

Table 1. Composition of high-strength low-carbon steel.

	Cu	C	Al	Ni	Si	Mn	Nb	P	S
wt.%	1.29	0.050	0.58	2.87	0.48	0.52	0.070	0.004	0.005
at.%	1.12	0.23	1.19	2.70	0.95	0.52	0.042	0.007	0.009

Balance is Fe.

crease in microhardness is attainable when NUCu-140-3 is aged at 550 °C. The added 2 h at 200 °C aging treatment yields an additional small increase in microhardness at the aging times studied. Both aging treatments attain peak microhardness at 0.25 h. The steels are overaged between 0.25 h and 1 h and reach a microhardness of 230.2 ± 4.7 VHN when aged 4 h at 550 °C, and 251.1 ± 3.9 VHN for the double-aged specimens. When compared to NUCu-170 and NUCu-140-1, which are aged at 500 °C, NUCu-140-3 attains peak microhardness at an earlier aging time with significantly smaller values. The change in microhardness is also less than for NUCu-140-1 and NUCu-170. Furthermore, unlike NUCu-170 and NUCu-140-1, we do not observe a microhardness plateau, which is most likely a result of faster kinetics at the higher aging temperature.

Evolution of the Cu-rich precipitate morphology is seen qualitatively in Fig. 2a–f, which depict subsets of an analyzed volume, $10 \times 10 \times 30$ nm^3 (3000 nm^3), each containing approximately 130000 atoms, for each aging time studied. The morphologies when aged at 550 °C are displayed in Fig. 2a–c and when aged at 550 °C plus 2 h at 200 °C in Fig. 2d–f. These figures illustrate that the precipitates grow and coarsen with increasing aging time. The precipitates, which are delineated with 10 at.% Cu isoconcentration surfaces, possess a spheroidal morphology.

Representative Cu-rich precipitates are presented in Fig. 3a–c when aged at 550 °C and in Fig. 4a–c when aged at 550 °C plus 2 h at 200 °C. The Cu atoms are orange, the Ni atoms are green, the Al atoms are teal, the Mn atoms are mustard, the Fe atoms are blue, and the Si atoms are gray, within the figures. The distribution of Ni, Al, and Mn atoms adjacent to the Cu atoms, at the α-Fe matrix precipitate/heterophase interface, is illustrated for each aging time and thermal treatment. Interfacial segregation is more pro-

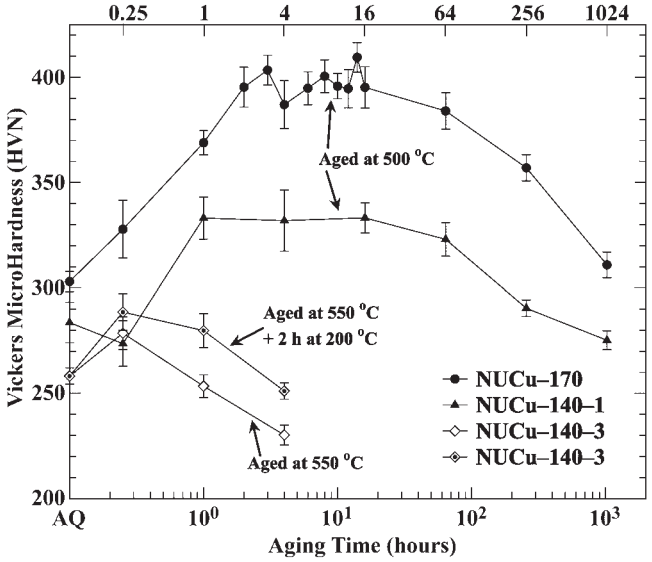

Fig. 1. Vickers microhardness (VHN) as a function of aging time when the NUCu-140-3 steel is aged at 550 °C (open diamonds) and 550 °C plus 2 h at 200 °C (open diamonds with solid circles); and when NUCu-140-1 (solid triangles), and NUCu-170 (solid circles) steel are aged at 500 °C.

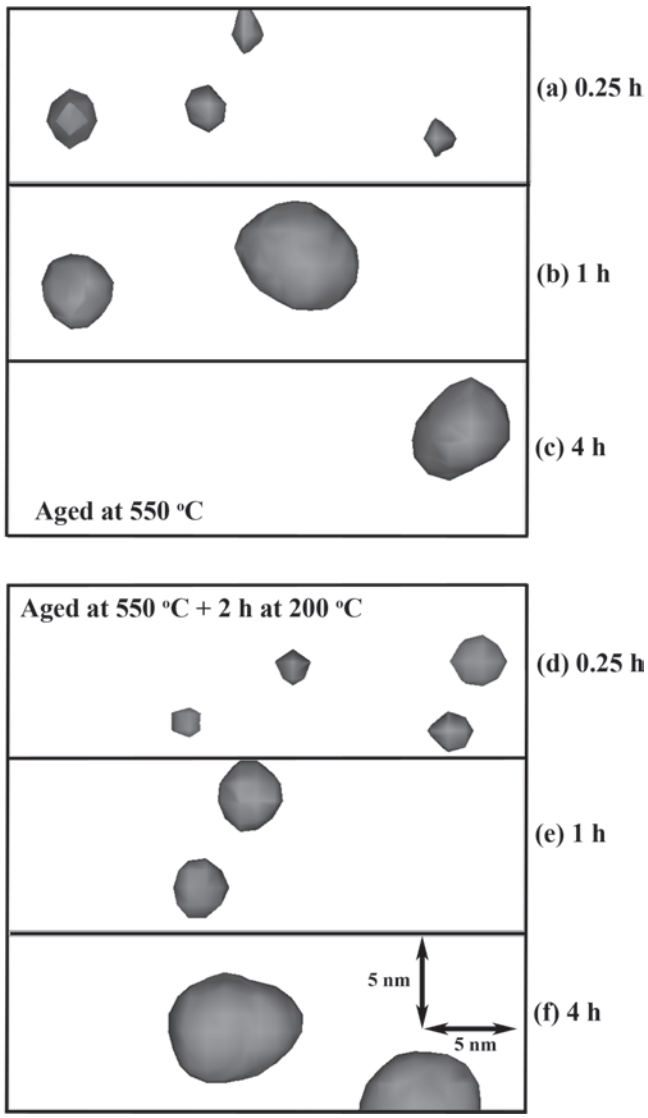

Fig. 2. Copper-rich precipitates as delineated by 10 at.% Cu isoconcentration surfaces, when the steel is aged at 550 °C for: (a) 0.25 h; (b) 1 h; (c) 4 h; and at 550 °C plus 2 h at 200 °C; (d) 0.25 h; (e) 1 h; and (f) 4 h. Each reconstruction, $10 \times 10 \times 30$ nm^3 (3000 nm^3), is a subset of an analyzed volume and contains approximately 130000 atoms.

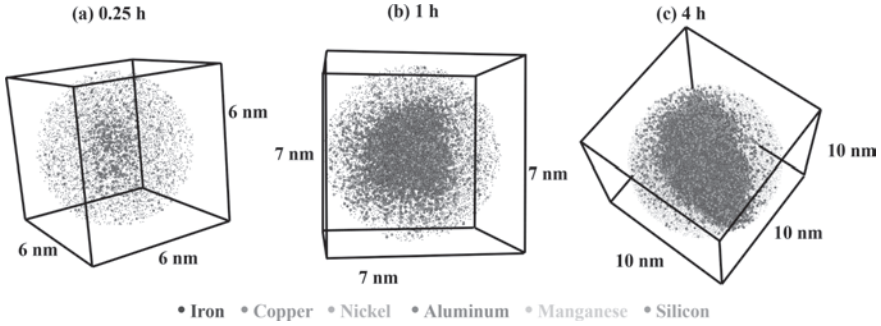

Fig. 3. Three-dimensional atom-probe tomographic reconstructions of representative precipitates when the steel is aged at 550 °C for: (a) 0.25 h; (b) 1 h; and (c) 4 h. The Cu, Ni, Al, and Mn atoms are shown as spheres (not to scale) allowing visualization of the precipitates and heterophase interfaces.

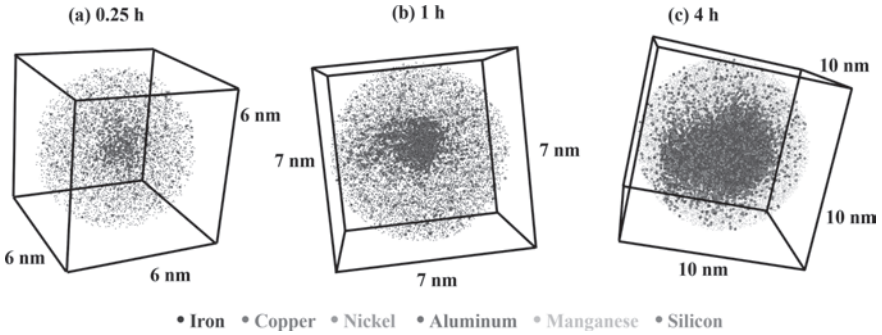

Fig. 4. Three-dimensional atom-probe tomographic reconstructions of representative precipitates when the steel is aged at 550 °C for: (a) 0.25 h; (b) 1 h; and (c) 4 h aged conditions and subsequently aged for 2 h at 200 °C. The Cu, Ni, Al, and Mn atoms are shown as spheres (not to scale) allowing visualization of the precipitates and heterophase interfaces.

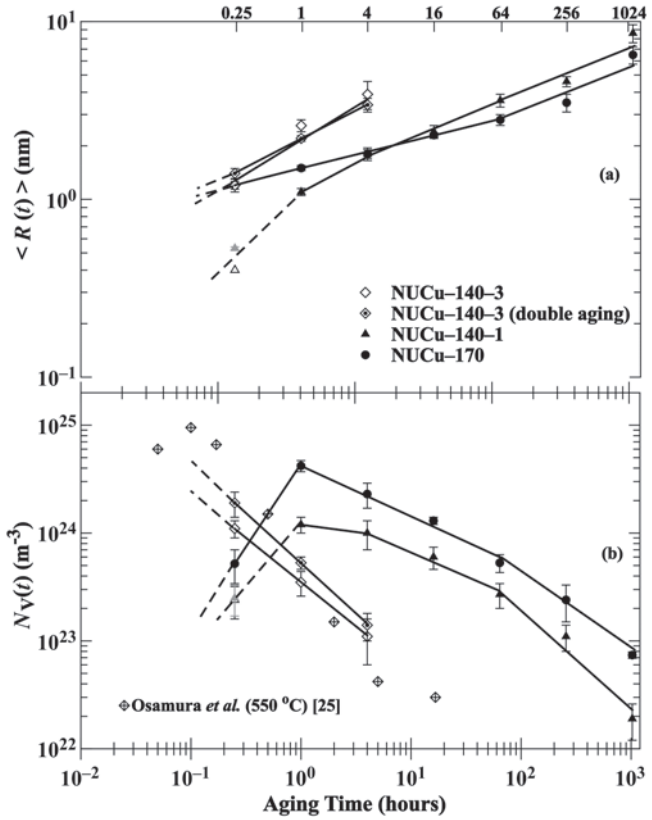

Fig. 5. The (a) mean precipitate radius, $\langle R(t)\rangle$; and (b) number density, $N_V(t)$, as a function of aging time for NUCu-140-3 when aged at 550 °C (open diamonds), at 550 °C plus 2 h at 200 °C (open diamonds with solid circles), and NUCu-140-1 (solid triangles) and NUCu-170 (solid circles), when aged at 500 °C. The values at 0.25 h for NUCu-140-1 are based on 4 at.% Cu isoconcentration surfaces (open triangles) or the envelope method (gray triangles). The data of Osamura et al. [25] for $N_V(t)$ is displayed (open diamonds with plus symbols) in (b).

nounced at certain locations around the precipitates. Other precipitates at the studied aging-states exhibit similar interfacial segregation and this observation is consistent with reported results in similar concentrated multicomponent steels [35–37] and in NUCu-170 [38] and NUCu-140-1 [39], where we discuss the observed interfacial segregation behavior in detail.

3.1.1. Coarsening

We first present results for when the steel is aged at 550 °C. At 0.25 h, the Cu-rich precipitates have formed within the matrix (Fig. 2a) with $\langle R(t)\rangle = 1.2 \pm 0.1$ nm (Fig. 5a), where the error is given by the standard error of the mean. At 0.25 h, $N_V(t) = (1.1 \pm 0.2) \times 10^{24}$ m^{-3} (Fig. 5b) and the volume fraction, ϕ, is equal to 0.5 ± 0.01 %, where the error is based on counting statistics for both quantities. The quantity $N_V(t)$ is a maximum at 0.25 h and subsequently decreases indicating the onset of coarsening. At 1 h, $\langle R(t)\rangle$ increases to 2.6 ± 0.2 nm, $N_V(t)$ decreases to $(3.5 \pm 0.9) \times 10^{23}$ m^{-3}, and ϕ is equal to 1.5 ± 0.01 %. Additional aging to 4 h yields $\langle R(t)\rangle = ; 3.9 \pm 0.7$ nm with $N_V(t) = (1.1 \pm 0.5) \times 10^{23}$ m^{-3}, and ϕ equal to 1.8 ± 0.01 %. The temporal dependency for $\langle R(t)\rangle$ is $t^{0.38\pm0.08}$, and for $N_V(t)$ it is $t^{-0.82\pm0.01}$ from 0.25 to 4 h.

When the steel is subjected to the double-aging treatment we measure slight variations in $\langle R(t)\rangle$ and $N_V(t)$. At 0.25 h, $\langle R(t)\rangle = 1.4 \pm 0.1$ nm, $N_V(t) = (1.9 \pm 0.5) \times 10^{24}$ nm^{-3}, and ϕ equal to 1.1 ± 0.02 %. The quantity $N_V(t)$ is a maximum at 0.25 h and subsequently decreases indicating the onset of coarsening. At 1 h, $\langle R(t)\rangle$ increases to 2.2 ± 0.1 nm, $N_V(t)$ decreases to $(5.3 \pm 0.7) \times 10^{23}$ m^{-3}, and ϕ is equal to 1.3 ± 0.01 %. Additional aging to 4 h yields $\langle R(t)\rangle = 3.4 \pm 0.3$ nm with $N_V(t) = (1.4 \pm 0.4) \times 10^{23}$ m^{-3}, and ϕ equal to 1.5 ± 0.01 %. The quantity $\langle R(t)\rangle$ is greater at 0.25 h but smaller at 1 and 4 h, compared to when the steel is aged only at 550 °C; whereas the quantity $N_V(t)$ is greater at 0.25 and 1 h but is the same at 4 h, within experimental uncertainty, see below. The temporal dependency for $\langle R(t)\rangle$ is $t^{0.32\pm0.01}$, and for $N_V(t)$ it is $t^{-0.93\pm0.01}$ from 0.25 to 4 h, which are similar, but not exactly the same, as the values when the steel is aged only at 550 °C, which we discuss in detail.

3.2. Temporal evolution of composition

The temporal evolution of the concentration profiles is presented in Figs. 6a–c and 7a–c. The figures represent the temporal evolution of the Cu, Fe, Ni, Al, Mn, and Si profiles from 0.25 to 4 h. These figures demonstrate clearly that the composition of the precipitates, α-Fe matrix precipitate/interfaces, and α-Fe matrix are temporally evolving. The observed interfacial segregation of Ni, Al, and Mn is localized (nonmonotonic), whereas the observed interfacial segregation of Cu, Fe, and Si is delocalized (monotonic).

3.2.1. Far-field matrix compositions

In this investigation the plateau-points [56] within the matrix (far-field) yield the α-Fe matrix concentrations (Table 2), where the plateau-region of the proxigram is delineated by utilizing the Fe concentration profiles as a fiducial marker. Only data points within the flat region of the profile, a minimum of 1.5 nm away from the heterophase interface and with $\pm 2\sigma < 0.4$ at.% are included.

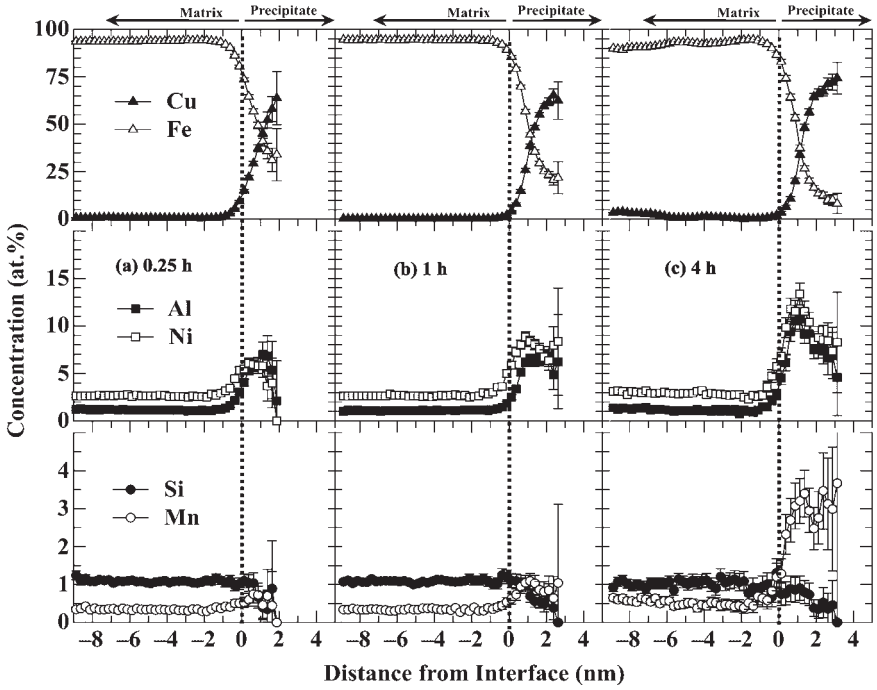

Fig. 6. Proxigram concentration profiles (at.%) for Cu, Fe, Ni, Al, Si, and Mn, when the steel is aged at 550 °C, for (a) 0.25 h; (b) 1 h; and (c) 4 h. The dotted vertical lines indicate the α-Fe matrix/precipitate interface.

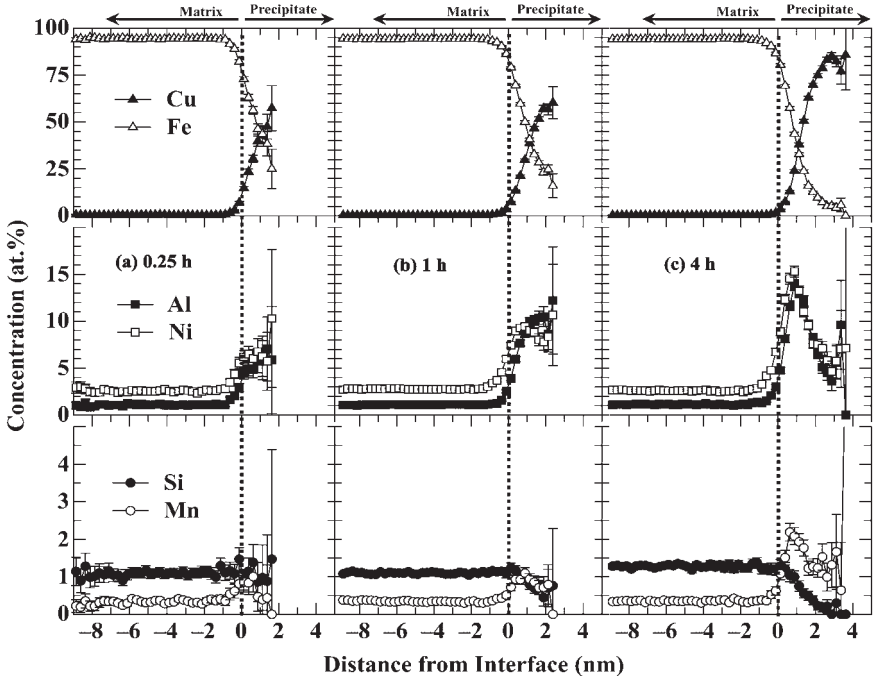

Fig. 7. Proxigram concentration profiles (at.%) for Cu, Fe, Ni, Al, Si, and Mn, when the steel is aged at 550 °C, for (a) 0.25 h; (b) 1 h; and (c) 4 h; and subsequently aged at 200 °C for 2 h. The dotted vertical lines indicate the α-Fe matrix/precipitate heterophase interface.

Table 2. Composition in at.% of the α-Fe matrix as determined by atom-probe tomography.

	Cu	C	Al	Ni	Si	Mn	Fe	Nb
0.25 h at 550 °C	0.8 ± 0.01	0.05 ± 0.002	1.2 ± 0.01	2.7 ± 0.02	1.1 ± 0.01	0.3 ± 0.006	93.9 ± 0.03	ND
1 h at 550 °C	0.3 ± 0.06	0.01 ± 0.01	1.1 ± 0.01	2.7 ± 0.02	1.1 ± 0.01	0.4 ± 0.006	94.5 ± 0.03	ND
4 h at 550 °C	0.3 ± 0.006	0.2 ± 0.005	1.0 ± 0.003	2.6 ± 0.003	1.1 ± 0.004	0.5 ± 0.008	94.4 ± 0.03	0.04 ± 0.002
0.25 h at 550 °C + 2 h at 200 °C	0.5 ± 0.02	0.02 ± 0.003	1.1 ± 0.03	2.6 ± 0.04	1.1 ± 0.03	0.3 ± 0.01	94.4 ± 0.06	ND
1 h at 550 °C + 2 h at 200 °C	0.3 ± 0.04	0.03 ± 0.001	1.1 ± 0.008	2.8 ± 0.01	1.1 ± 0.007	0.4 ± 0.004	94.2 ± 0.02	0.002 ± 0.001
4 h at 550 °C + 2 h at 200 °C	0.4 ± 0.2	0.03 ± 0.02	1.1 ± 0.3	2.6 ± 0.4	1.3 ± 0.4	0.4 ± 0.2	94.2 ± 0.7	ND

ND = Not detected.

The concentration of Cu decreases within the α-Fe matrix for both thermal treatments. The concentrations of Fe and Si are consistently greater than the nominal concentration for the aging times studied for both thermal treatments. Niobium is not detected within the α-Fe matrix, with the exception of the 4 h at 550 °C and 1 h at 550 °C plus 2 h at 200 °C aged states; whereas C is detected at a reduced concentration when compared to its nominal value. In the NUCu steels, Nb is not normally detected by APT due to the existence of NbC precipitates at a smaller number density ($\leq 10^{22}$ m^{-3}) than the Cu-rich precipitates [2, 57, 58]. Similarly, C is detected at smaller concentrations within the α-Fe matrix due to the presence of NbC precipitates, cementite (Fe_3C) [36], and segregation at grain-boundaries [36]. In the 4 h at 550 °C and 1 h at 550 °C plus 2 h at 200 °C aged states the presence of a NbC precipitate at the boundary of an analyzed volume yields the measured Nb concentration.

3.2.2. Composition of the Cu-rich precipitate cores

We first present results for when the steel is aged at 550 °C. At 0.25 h of aging the precipitate cores are Cu-rich (48.5 ± 2.0 at.%) but also contain significant quantities of Fe, Ni, and Al, and smaller quantities of Si and Mn (Table 3). The Cu concentration increases as a result of further aging, achieving a value of 72.0 ± 1.4 at.% at 4 h. The Fe concentration decreases concomitantly from 38.8 ± 2.0 at.% at 0.25 h to 9.9 ± 1.6 at.% at 4 h. The concentrations of Ni and Mn increase, whereas that of Al is constant within experimental uncertainty. At the aging times studied the Ni, Al, and Mn concentrations are equal to or greater than the nominal concentrations. The Si concentration is approximately constant but is less than the nominal concentration at the aging times studied. Carbon and Nb are not detected inside the precipitate cores, within the prescribed experimental uncertainty.

When the steel is subjected to the double-aging treatment we measure similar, but not exactly the same concentrations within the precipitate cores (Table 3). The concentrations of Cu and Mn increase whereas Fe decreases, following similar trends as when the steel is aged only at 550 °C. The concentration of Si, however, displays a continuous decrease. The concentrations of Ni and Al exhibit a more complicated behavior. Both elements are, however, consistently found enhanced within the cores at the aging times studied. Carbon and Nb are not detected inside the precipitate cores, within the prescribed experimental uncertainty.

For both thermal treatments the concentrations of Ni, Al, and Mn are affected by the bccCu → 9RCu → 3RCu → fcc epsilon-Cu phase changes in the precipitates [14, 16, 17] and the formation of a Ni–Al–Mn phase at the heterophase interfaces, which has been discussed in detail [38, 43].

3.2.3. Composition of α-Fe matrix/precipitate interfaces

The composition of the α-Fe matrix/precipitate interfaces is also displayed in Figs. 6a–c and 7a–c. The heterophase in-

Table 3. Composition in at.% of the Cu-rich precipitate cores as determined by atom-probe tomography.

	Cu	C	Al	Ni	Si	Mn	Fe	Nb
0.25 h at 550 °C	48.5 ± 2.0	0.04 ± 0.04	6.7 ± 1.0	5.0 ± 0.9	0.4 ± 0.3	0.5 ± 0.3	38.8 ± 2.0	ND
1 h at 550 °C	60.1 ± 1.1	ND	6.8 ± 0.6	6.8 ± 0.6	0.5 ± 0.2	0.8 ± 0.2	24.2 ± 1.0	ND
4 h at 550 °C	72.0 ± 1.4	ND	6.5 ± 1.3	8.1 ± 1.5	0.4 ± 0.3	3.1 ± 0.9	9.9 ± 1.6	0.07 ± 0.07
0.25 h at 550 °C +2 h at 200 °C	42.1 ± 2.2	ND	6.0 ± 1.0	6.6 ± 1.1	0..9 ± 0.4	0.4 ± 0.3	44.0 ± 2.2	ND
1 h at 550 °C + 2 h at 200 °C	57.2 ± 1.5	0.04 ± 0.03	10.1 ± 0.9	8.0 ± 0.8	0.5 ± 0.2	0.7 ± 0.2	23.4 ± 1.2	ND
4 h at 550 °C + 2 h at 200 °C	83.4 ± 1.0	0.02 ± 0.02	4.5 ± 0.6	5.5 ± 0.6	0.2 ± 0.1	1.2 ± 0.3	5.1 ± 0.6	ND

ND = Not detected.

Table 4. Composition in at.% of the precipitate/α-Fe matrix heterophase interfaces as determined by atom-probe tomography.

	Cu	C	Al	Ni	Si	Mn	Fe	Nb
0.25 h at 550 °C	3.8 ± 0.07	0.06 ± 0.01	1.7 ± 0.04	3.4 ± 0.06	1.1 ± 0.04	0.4 ± 0.02	89.5 ± 0.1	ND
1 h at 550 °C	9.8 ± 0.1	0.01 ± 0.005	2.7 ± 0.07	5.0 ± 0.1	1.0 ± 0.04	0.6 ± 0.03	80.9 ± 0.2	ND
4 h at 550 °C	20.6 ± 0.4	0.1 ± 0.03	5.5 ± 0.2	7.5 ± 0.2	0.8 ± 0.08	1.9 ± 0.1	63.5 ± 0.4	0.2 ± 0.01
0.25 h at 550 °C + 2 h at 200 °C	5.2 ± 0.2	0.01 ± 0.01	2.1 ± 0.1	3.8 ± 0.1	1.1 ± 0.08	0.5 ± 0.05	87.2 ± 0.2	ND
1 h at 550 °C + 2 h.at 200 °C	8.1 ± 0.08	0.03 ± 0.005	3.2 ± 0.05	5.2 ± 0.06	1.1 ± 0.03	0.5 ± 0.02	81.8 ± 0.1	0.003 ± 0.001
4 h at 550 °C + 2 h at 200 °C	17.0 ± 0.1	0.03 ± 0.007	5..4 ± 0.08	7.3 ± 0.1	1.1 ± 0.04	1.0 ± 0.04	68.2 ± 0.2	ND

ND = Not detected.

terfacial region, at as early as 0.25 h of aging for both thermal treatments, is enriched in Cu, Ni, Al, and Mn but is depleted in Fe (Table 4). We first present results for when the steel is aged at 550 °C. The Ni peak concentration within the interfacial region (6.1 ± 0.5 at.%) is located at a distance of 0.375 nm close to the Mn peak concentration (0.7 ± 0.2 at.%), which is found at a distance of 0.625 nm. The Al peak-concentration (7.0 ± 1.3 at.%) is found toward the center of the precipitate at 1.125 nm. At 1 h, the Ni (8.9 ± 0.5 at.%) peak-concentration is found at 0.875 nm, the Mn (1.1 ± 0.2 at.%) peak is located at a distance of 1.125 nm, while the Al peak concentration (7.1 ± 0.8 at.%) is at a distance of 1.875 nm. Nickel, Al, and Mn enhancements are also found at the center of the precipitates but with greater experimental uncertainties. At 4 h, distinct enhancements of Ni (13.4 ± 1.1 at.%) and Al (10.7 ± 1.0 at.%) are found collocated at a distance of 1.125 nm. Manganese exhibits enhancement from the interfacial region to the precipitate core, between 0.875 and 3.125 nm. Two Mn peaks are observed, 3.4 ± 0.6 at.% at 1.375 nm, near the Ni and Al peaks, and 3.5 ± 1.0 at.% at 2.375 nm, toward the center of the precipitate. Silicon is also found within the heterophase interfacial region at a concentration of approximately 0.8–1.1 at.%. Niobium is not detected, with the exception of the 4 h at 550 °C state, whereas C is detected at a reduced concentration when compared to its nominal value.

When the steel is subjected to the double-aging treatment we observe qualitatively similar results. At 0.25 h, a Ni peak of 6.5 ± 0.8 at.% is located at a distance of 0.375 nm. A second Ni enhancement is observed at 1.625 nm but with significantly greater experimental uncertainty. The Mn-peak (1.0 ± 0.4 at.%) is located close to the Ni-peak at a distance of 0.625 nm, whereas the Al-peak (7.0 ± 1.7 at.%) is found toward the center at 1.375 nm. At 1 h, the Ni (9.4 ± 0.4 at.%) peak-concentration is collocated with the Mn (1.1 ± 0.1 at.%) peak at a distance of 0.875 nm, while the Al peak-concentration (10.5 ± 1.1 at.%) is at a distance of 1.875 nm. Nickel and Al enhancements are also found at the center of the precipitates but with greater experimental uncertainties. At 4 h, a distinct enhancement of Ni, Al, and Mn is observed at the heterophase interfaces, with peak concentrations of 15.3 ± 0.6 at.% for Ni and 13.8 ± 0.6 at.% for Al at a distance of 0.875 nm. The Mn peak-concentration of 2.2 ± 0.2 at.% is found at a distance of 0.625 nm. Silicon is also found within the heterophase interfacial region at an approximately constant concentration of 1.1 at.%. Niobium is not detected, with the exception of the 1 h at 550 °C plus 2 h at 200 °C aging state, whereas C is detected at a reduced concentration when compared to its nominal value.

The temporal evolution of the Ni, Al, and Mn concentrations within the heterophase interfaces is related to that within the precipitate cores and is possibly affected by the phase changes of the precipitate as has been discussed [38, 43].

3.2.4. Partitioning ratios

The temporal evolution of the partitioning ratio [54],

$$\kappa_i^{\mathrm{ppt./mat.}}(t) = \frac{C_i^{\mathrm{ppt.}}(t)}{C_i^{\mathrm{mat.,ff}}(t)} \tag{3}$$

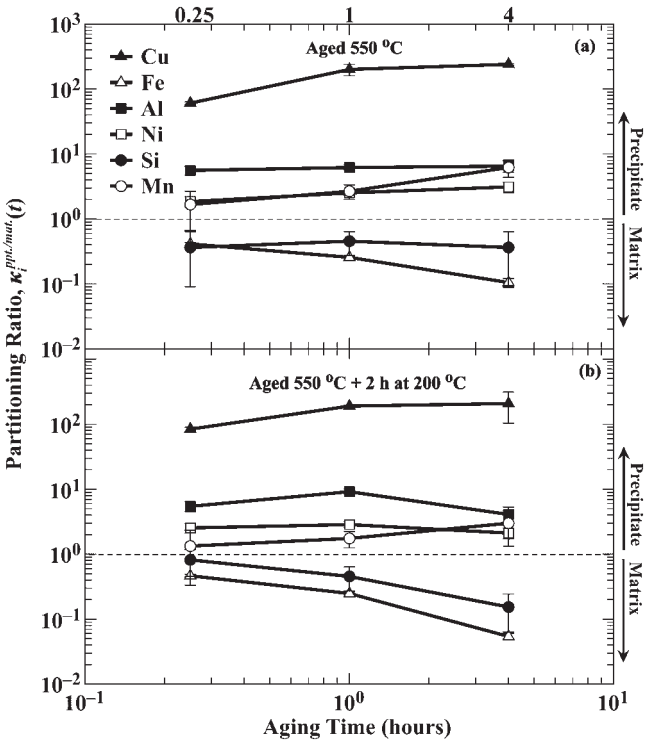

Fig. 8. Partitioning ratios, $\kappa_i^{\mathrm{ppt./mat.}}(t)$, of the concentrated multicomponent Fe–Cu steel as a function of aging time, when aged between 0.25 and 4 h at: (a) 550 °C; and (b) 550 °C plus 2 h at 200 °C. The horizontal dashed lines indicate the division between the precipitate and matrix phases.

is displayed in Fig. 8a when aged at 550 °C and when aged at 550 °C plus 2 h at 200 °C, Fig. 8b. The standard error for κ_i is determined by standard error-propagation methods of the concentration errors [59]. Figure 8 illustrates clearly that Cu partitions to the precipitates, whereas Fe and Si partition to the matrix for both thermal treatments. The Si behavior in Fig. 8a demonstrates slightly slower partitioning kinetics than that displayed in Fig. 8b. Nickel, Al, and Mn exhibit similar behavior, preferring the Cu-rich precipitate phase from 0.25 to 4 h. The proximity of Al and Mn, though, to the dashed-line separating precipitate and matrix-phases indicates that all three elements partition to the interfacial region. The partitioning ratio for Mn demonstrates very similar behavior in both figures.

4. Discussion

4.1. Morphology

The difference in microhardness between the two thermal treatments is possibly a result of further nucleation of precipitates. The results presented in Table 2 indicate that after 0.25 h of aging at 550 °C the Cu concentration within the α-Fe matrix is still evolving temporally, assuming an equilibrium concentration of approximately 0.1–0.2 at.% as determined for NUCu-170 [38] and NUCu-140-1 [39]. Subsequent aging for 2 h at 200 °C reduces the Cu concentration further with an increased value of $N_V(t)$ indicating that additional precipitate nucleation is occurring. The quantity $\langle R(t) \rangle$ is slightly greater, however, which suggests that some growth is occurring for the existing precipitates. A smaller difference in $N_V(t)$ is observed between 1 and 4 h, while the values for $N_V(t)$ are the same within experimental

uncertainty. We ascribe this to reduced nucleation current during the double-aging treatment, as longer initial aging at 550 °C reduces the Cu concentration within the matrix. The steady-state nucleation current (number of nuclei per unit volume per unit time), J, in classical nucleation theory (CNT), is given by [60],

$$J \propto \exp\left(\frac{-W_R^*}{k_B T}\right) \quad (4)$$

where W_R^* is the critical net reversible work required for the formation of a critical spherical nucleus, k_B is Boltzmann's constant, and T is the absolute temperature in Kelvin. The quantity W_R^* is the nucleation barrier, which is inversely proportional to the square of the volume free energy change, ΔF_V, involved in forming a nucleus, where F is the Helmholtz free energy. The quantity, ΔF_V, is dependent on the matrix supersaturation, which if smaller, reduces J. Furthermore, growth and coarsening of existing precipitates also reduces the value of $N_V(t)$.

The spheroidal morphology of the precipitates observed for both thermal treatments is consistent with that observed for NUCu-170 [38] and NUCu-140-1 [39] at shorter aging times.

4.2. Coarsening kinetics

The coarsening kinetics of NUCu-140-3 is faster than that of NUCu-170 [38] and NUCu-140-1 [39]. The onset of coarsening is observed for NUCu-140-3 at approximately 0.25 h. The double-aging treatment for NUCu-140-3 does not change this observation. The onset of coarsening is observed for NUCu-140-1, which is aged at 500 °C, at 4 h, whereas the onset of coarsening for NUCu-170 is 1 h, which is also aged at 500 °C. Additionally, NUCu-170 possesses a greater Cu concentration, 1.82 at.%.

The difference in power-law time exponents for $\langle R(t)\rangle$ is seen in Fig. 5a. For NUCu-140-3 aged at 550 °C we observe a temporal dependency of $t^{0.38\pm0.08}$, which is close, but not exactly equal to the UO model prediction of 1/3. When this steel is subjected to the double-aging treatment we observe a temporal dependency of $t^{0.32\pm0.01}$, which is in approximate agreement with the model prediction. We do not observe temporal dependencies for $\langle R(t)\rangle$ indicating a distinct nucleation regime nor do we observe a short diffusion-controlled growth regime [61, 62] as in NUCu-140-1 [39]. Furthermore we also do not observe temporal dependencies for $\langle R(t)\rangle$ indicating a transition regime from growth to coarsening [61] as is the case for NUCu-170 [38]. Our results for NUCu-140-3 demonstrate that at 550 °C the temporal dependencies for $\langle R(t)\rangle$ agree with the UO model as early as 0.25 h, which is unlike NUCu-170 and NUCu-140-1, where agreement occurs only at times ≥ 64 h. Additionally, our results for aging at 550 °C more closely concur with the results for binary Fe–Cu [15, 44] and ternary Fe–Cu–Ni [45] carbon-free alloys aged between 600 and 830 °C.

The difference in power-law time exponents for $N_V(t)$ is observable in Fig. 5b. For NUCu-140-3 aged at 550 °C we observe a temporal dependency of $t^{-0.82\pm0.01}$, whereas we observe a power-law time exponent of $t^{-0.93\pm0.01}$ for the double-aging treatment. Both values are less than the UO model prediction of –1, indicating a slower rate of coarsening. Both dependencies are, however, greater than the values reported for NUCu-170 [38] and NUCu-140-1 [39], even at times ≥ 64 h, indicating that NUCu-140-3 is coarsening more rapidly when aged at 550 °C as anticipated.

In Fig. 5b we plot the reported data for $N_V(t)$ for a quaternary Fe–Cu–Ni–Mn low-carbon alloy [23] aged at 550 °C for comparison with our results. We have previously compared literature data with our results for aging at 500 °C [39]. Osamura et al.'s data [23] was obtained from SANS measurements (open diamonds with pluses) and indicates coarsening commencing at 0.1 h for their alloy. The calculated temporal dependency of $t_{0.1-16.67h}^{-0.98\pm0.12}$ for the data of Osamura et al., signifies a faster rate of coarsening than NUCu-140-3, which we attribute to the smaller solute concentrations and less complex precipitation kinetics of this alloy [23]. The observed variation is also possibly due to differences in measuring techniques.

4.3. Composition of the Cu-rich precipitates and partitioning

We measure an Fe concentration of 38.8 ± 2.0 at.% for aging only at 550 °C and 44.0 ± 2.2 at.% for aging at 550 °C plus 2 h at 200 °C, when the Cu-rich precipitates are smaller than 2 nm in radius, Fig. 5a, which possess a bcc structure [5, 16, 25]. This is consistent with our observations for NUCu-170 [38], where we measure between 39.9 ± 4.2 and 27.6 ± 2.1 at.% Fe. These values are, however, greater than our observations for NUCu-140-1 [39], where we measured between 27.8 ± 3.1 and 24.2 ± 1.4 at.% Fe, and earlier observations for NUCu-140-1, where the Fe concentration of the precipitates is ~25 at.% at peak microhardness [2]. Both NUCu-170 and NUCu-140-1 were aged at 500 °C; additionally, NUCu-170 contains a greater alloying concentration. The differences that occur between APT and SANS measurements of the Fe concentrations in precipitates <2 nm in radius are discussed in Ref. [38].

We also measure a Cu concentration of 48.5 ± 2.0 at.% for aging only at 550 °C and 42.1 ± 2.2 at.% for aging at 550 °C plus 2 h at 200 °C, when the Cu-rich precipitates are smaller than 2 nm in radius. This is similar to the concentrations observed for NUCu-170, where the precipitates contain between 44.6 ± 3.1 and 53.5 ± 2.3 at.% Cu [38], which is slightly less than that of NUCu-140-1, where we measure between 50.5 ± 3.5 and 56.6 ± 1.6 at.% Cu. The precipitates also contain quantities of Ni, Al, Mn, and Si, which are similar to those found in NUCu-170 [38], NUCu-140-1 [39], earlier atom-probe measurements for model ternary [9, 10] and multicomponent Fe–Cu based alloys [36], and recent phase-field simulations of model quaternary Fe–Cu–Ni–Mn alloys [29, 30], and Langer–Schwartz simulations of model Fe–Cu–Ni and Fe–Cu–Mn alloys [34].

4.4. Heterophase interfacial segregation of Ni–Al–Mn

The observed segregation of Ni, Al, and Mn at heterophase interfaces in NUCu-140-3 is comparable to that in NUCu-170 [38] and NUCu-140-1 [39]. We discuss in detail the formation of a $Ni_{0.5}(Al_{0.5-x}Mn_x)$ phase enveloping the Cu-rich precipitates [38]. In NUCu-170 the stoichiometric ratio for Ni : Al : Mn is observed to evolve temporally acheivining a ratio of 0.51 : 0.41 : 0.08 at 1024-h. This ratio is sug-

Table 5. Temporal evolution of Ni : Al : Mn stoichiometric ratio within the heterophase interfaces as a function of aging time.

	Ni :	Al :	Mn
0.25 h at 550 °C	0.61	0.31	0.07
1 h at 550 °C	0.60	0.33	0.07
4 h at 550 °C	0.50	0.37	0.13
0.25 h at 550 °C + 2 h at 200 °C	0.60	0.32	0.08
1 h at 550 °C + 2 h at 200 °C	0.58	0.36	0.06
4 h at 550 °C + 2 h at 200 °C	0.53	0.40	0.07

gestive of a NiAl-type B2 phase. And we performed synchrotron radiation studies at the Advanced Photon Source (APS), Argonne, Illinois, which demonstrate that this shell does indeed have the B2 structure [43]. Comparable to NUCu-170 and NUCu-140-1 the Ni : Al : Mn stoichiometric ratio evolves temporally in NUCu-140-3 (Table 5). The values are similar, but not exactly the same, as NUCu-170 [38] and NUCu-140-1 [39]. The observed variations are attributable to differences in aging temperature, which should affect the kinetics of forming the $Ni_{0.5}(Al_{0.5-x}Mn_x)$ phase.

5. Conclusions

The coarsening behavior of Cu-rich precipitates in a concentrated multicomponent Fe–Cu based steel containing 1.12 at. % Cu (Table 1) is studied experimentally. This steel is denoted NUCu-140-3 (140 designates the yield strength in ksi and 3 the heat number), is aged at 550 °C for times between 0.25 and 4 h. A second set of specimens received the same thermal treatment and is further aged for 2 h at 200 °C. The aging times investigated are relevant for technological applications of this steel. Our investigation results in the following findings:

1. The temporal dependencies for the spherical volume equivalent mean radius, $\langle R(t)\rangle$, are $t^{0.38\pm0.08}$ when aged only at 550 °C and $t^{0.32\pm0.01}$ for the double-aging treatment, which are both in approximate agreement with the Umantsev–Olson (UO) coarsening model prediction of 1/3.
2. The number density of precipitates, $N_V(t)$, decreases from $(1.1 \pm 0.2) \times 10^{24}$ m^{-3} at 0.25 h of aging to $(1.1 \pm 0.5) \times 10^{23}$ at 4 h with a temporal dependency of $t^{-0.82\pm0.01}$, when aged only at 550 °C. For the double aging treatment, $N_V(t)$ decreases from $(1.9 \pm 0.5) \times 10^{24}$ m^{-3} to $(1.4 \pm 0.4) \times 10^{23}$ m^{-3} with a temporal dependency of $t^{-0.93\pm0.01}$. The coarsening power-law exponents indicate a slower rate of coarsening than the UO model predicted value of –1, which indicate that a quasi-stationary-state is not achieved.
3. An increase in $N_V(t)$ is observed after aging at 550 °C plus 2 h at 200 °C when compared to aging specimens only at 550 °C. The observed difference in the $N_V(t)$ values decrease from 0.25 to 4 h, where the $N_V(t)$ values are identical, within experimental uncertainty. This increase at 0.25 h is a result of greater quantities of Cu remaining in the matrix at shorter aging times, Table 2, which most likely results in the formation of additional nuclei due to the larger supersaturation.
4. Copper partitions to the precipitate core, whereas Ni, Al, and Mn partition to the heterophase interfaces, and Fe and Si partition to the α-Fe matrix for both thermal treatments. The temporal evolution of Ni, Al, and Mn concentrations at the heterophase interfaces are localized (nomonotonic).
5. The formation of a $Ni_{0.5}(Al_{0.5-x}Mn_x)$ phase at the Cu-rich α-Fe matrix precipitate interfaces is observed consistently in the steels studied: it envelops the precipitates.
6. From the above conclusions and our earlier studies on NUCu-170 and NUCu-140-1 it is clear that it is difficult to describe the temporal coarsening behavior of a concentrated multicomponent alloy using classical coarsening models, which do not allow for the temporal evolution of a precipitate's chemical composition. An alternative approach is to utilize PrecipiCalc [63], which is a more general approach to the problem of phase decomposition that includes thermodynamic and mobility data bases. There are not yet, however, adequate thermodynamic and mobility databases that would allow its use for the Fe–Cu based steel we report on in this article.
7. The results presented in this article demonstrate unequivocally that the composition of Cu-rich precipitates in Fe–Cu based steels is kinetically determined as the approach to the equilibrium composition is both temperature and time-dependent. The time to achieve the equilibrium thermodynamic composition is temperature dependent and therefore the precipitates may not achieve their equilibrium composition if the aging time is not sufficiently long.

This research is supported by the Office of Naval Research (N00014-03-1-0252), Drs. Julie Christodoulou and W. Mullins grant officers. Atom-probe tomographic analyses were performed at the Northwestern University Center for Atom-Probe Tomography (NUCAPT), and the LEAP tomograph was purchased with funding from the NSF-MRI (DMR-0420532, Dr. Charles Bouldin, monitor) and ONR-DURIP (N00014-0400798, Dr. Julie Christodoulou, monitor) programs. Additionally, the LEAP tomograph was enhanced in late April 2006 with a picosecond laser (wavelength = 552 nm) with funding from ONR-DURIP (N0014-06-1-0539, Dr. Julie Christodoulou, monitor). This work made use of Central Facilities supported by the MRSEC program of the National Science Foundation (DMR-0520513) at the Materials Research Center of Northwestern University. We thank Professor Emeritus Morris E. Fine, Research Professor Semyon Vaynman, and Research Assistant Professor Dieter Isheim for stimulating discussions, and to DI for managing NUCAPT.

References

[1] T.W. Montemarano, B.P. Sack, J.P. Gudas, M.G. Vassilaros, H.H. Vanderveldt: J. Ship Prod. 2 (1986) 145.
[2] S. Vaynman, D. Isheim, R.P. Kolli, S.P. Bhat, D.N. Seidman, M.E. Fine: Metall. Mater. Trans. A 39 (2008) 363. DOI:10.1007/s11661-007-9417-x
[3] S.K. Dhua, D. Mukerjee, D.S. Sarma: Metall. Mater. Trans. A 32 (2001) 2259. DOI:10.1007/s11661-001-0201-z
[4] E.J. Czyrycka, R.E. Link, R.J. Wong, D.A. Aylor, T.W. Montemarano, J.P. Gudas: Nav. Eng. J. 102 (1990) 63. DOI:10.1111/j.1559-3584.1990.tb02632.x
[5] S.K. Lahiri, D. Chandra, L.H. Schwartz, M.E. Fine: Trans. Metall. Soc. AIME 245 (1969) 1865.
[6] S.R. Goodman, S.S. Brenner, J.R. Low Jr.: Metall. Trans. 4 (1973) 2363. DOI:10.1007/BF02669376
[7] A. Youle, B. Ralph: Met. Sci. J. 6 (1972) 149.
[8] S.R. Goodman, S.S. Brenner, J.R. Low Jr.: Metall. Trans. 4 (1973) 2371. DOI:10.1007/BF02669377
[9] G.M. Worrall, J.T. Buswell, C.A. English, M.G. Hetherington, G.D.W. Smith: J. Nucl. Mater. 148 (1987) 107. DOI:10.1016/0022-3115(87)90525-3
[10] P.J. Pareige, K.F. Russell, M.K. Miller: Appl. Surf. Sci. 94/95 (1996) 362. DOI:10.1016/0169-4332(95)00398-3
[11] N. Maruyama, M. Sugiyama, T. Hara, H. Tamehiro: Mater. Trans. JIM 40 (1999) 268.

[12] M.K. Miller, K.F. Russell K.F., P.J. Pareige, M.J. Starink, R.C. Thomson: Mater. Sci. Eng. A 250 (1998) 49. DOI:10.1016/S0921-5093(98)00535-8
[13] M. Charleux, F. Livet, F. Bley, F. Louchet, Y. Bréchet: Philos. Mag. A 73 (1996) 883. DOI:10.1080/01418619608243694
[14] E. Hornbogen, R.C. Glenn: Trans. Metall. Soc. AIME 218 (1960) 1064.
[15] G.R. Speich, R.A. Oriani: Trans. Metall. Soc. AIME 233 (1965) 623.
[16] P.J. Othen, M.L. Jenkins, G.D.W. Smith: Philos. Mag. A 70 (1994) 1. DOI:10.1080/01418619408242533
[17] P.J. Othen, M.L. Jenkins, G.D.W. Smith, W.J. Phythian: Philos. Mag. Lett. 64 (1991) 383. DOI:10.1080/09500839108215121
[18] R. Monzen, M.L. Jenkins, A.P. Sutton: Philos. Mag. A 80 (2000) 711. DOI:10.1080/01418610008212077
[19] A. Deschamp, M. Militzer, W.J. Poole: ISIJ Int. 41 (2001) 196. DOI:10.2355/isijinternational.41.196
[20] T. Watanabe: Tetsu To Hagane 61 (1975) 2456.
[21] R. Kampmann, R. Wagner: Phase Transformations in Fe–Cu–Alloys – SANS-Experiments and Theory. in C. Janot, W. Petry, D. Richter, T. Springer T. editors. Atomic Transport and Defects in Metals by Neutron Scattering, vol. 10. Berlin: Springer-Verlag (1986) 73.
[22] K. Osamura, H. Okuda, K. Asano, M. Furusaka, K. Kishida, F. Kurosawa: ISIJ Int. 34 (1994) 346. DOI:10.2355/isijinternational.34.346
[23] K. Osamura, H. Okuda, M. Ochiai, M. Takashima, K. Asano, M. Furusaka, K. Kishida, F. Kurosawa: ISIJ Int. 34 (1994) 359. DOI:10.2355/isijinternational.34.359
[24] K. Osamura, H. Okuda, M. Takashima, K. Asano, M. Furusaka: Mater. Trans. JIM 34 (1993) 305.
[25] S. Pizzini, K.J. Roberts, W.J. Phythian, C.A. English, G.N. Greaves: Philos. Mag. Lett. 61 (1990) 223. DOI:10.1080/09500839008202362
[26] F. Maury, N. Lorenzelli, M.H. Mathon, C.H. de Novion, P. Lagarde: J. Phys.: Condens. Mater. 6 (1994) 569. DOI:10.1088/0953-8984/6/2/027
[27] C. Zhang, N. Enomoto, T. Yamashita, N. Sano: Metall. Mater. Trans. A 35 (2004) 1263. DOI:10.1007/s11661-004-0300-8
[28] F. Soisson, A. Barbu, G. Martin: Acta Mater. 44 (1996) 3789. DOI:10.1016/1359-6454(95)00447-5
[29] T. Koyama, K. Hashimoto, H. Onodera: Mater. Trans. 47 (2006) 2765. DOI:10.2320/matertrans.47.2765
[30] T. Koyama, H. Onodera: Mater. Trans. 46 (2005) 1187. DOI:10.2320/matertrans.46.1187
[31] J. Liu, A. van de Walle, M.D. Asta: Phys. Rev. B 72 (2005) 144109. DOI:10.1103/PhysRevB.72.144109
[32] J.J. Blackstock, G.J. Ackland: Philos. Mag. A 81 (2001) 2127. DOI:10.1080/01418610108217139
[33] T. Nagano, M. Enomoto: Scripta Mater. 55 (2006) 223. DOI:10.1016/j.scriptamat.2006.04.015
[34] C. Zhang, M. Enomoto: Acta Mater. 54 (2006) 4183. DOI:10.1016/j.actamat.2006.05.006
[35] D. Isheim, M.S. Gagliano, M.E. Fine, D.N. Seidman: Acta Mater. 54 (2006) 841. DOI:10.1016/j.actamat.2005.10.023
[36] D. Isheim, R.P. Kolli, M.E. Fine, D.N. Seidman: Scripta Mater. 55 (2006) 35. DOI:10.1016/j.scriptamat.2006.02.040
[37] D. Isheim, D.N. Seidman: Surf. Interface Anal. 36 (2004) 569. DOI:10.1002/sia.1703
[38] R.P. Kolli, D.N. Seidman: Acta Mater. 56 (2008) 2073. DOI:10.1016/j.actamat.2007.12.044
[39] R.P. Kolli, R.M. Wojes, S. Zaucha, D.N. Seidman: Int. J. Mater. Res. 99(5) (2008) 513.
[40] I.M. Lifshitz, V.V. Slyzov: J. Phys. Chem. Solids 19 (1961) 35. DOI:10.1016/0022-3697(61)90054-3
[41] C. Wagner: Electrochem. 65 (1961) 581.
[42] A. Umantsev, G.B. Olson: Scripta Metall. Mater. 29 (1993) 1135. DOI:10.1016/0956-716X(93)90191-T
[43] R.P. Kolli, Z. Mao, D.T. Keane, D.N. Seidman: Appl. Phys. Lett. 91 (2007) 241903. DOI:10.1063/1.2820378
[44] R. Monzen, K. Takada, K. Matsuda: Z. Metallkd. 94 (2003) 1241.
[45] R. Monzen, K. Takada, C. Watanabe: ISIJ Int. 44 (2004) 442. DOI:10.2355/isijinternational.44.442
[46] S. Vaynman, M.E. Fine, S. Lee, H.D. Espinosa: Scripta Mater. 55 (2006) 351. DOI:10.1016/j.scriptamat.2006.04.029
[47] S. Vaynman, D. Isheim, M.E. Fine, D.N. Seidman, S.P. Bhat, in: Recent advances in high-strength, low-carbon, precipitation-strengthened ferritic steels. Materials Science and Technology 2004, vol. 1, AIST and TMS, New Orleans, Louisiana: (2004).
[48] T.T. Tsong: Atom-probe field ion microscopy., Cambridge University Press, Cambridge, U.K. (1990).
[49] M.K. Miller, Atom Probe Tomography. New York: Kluwer Academic/Plenum Publishers, New York (2000).
[50] T.F. Kelly, T.T. Gribb, J.D. Olson, R.L. Martens, J.D. Shepard, S.A. Wiener, T.C. Kunicki, R.M. Ulfig, D.R. Lenz, E.M. Strennen, F. Oltman, J.H. Bunton, D.R. Strait: Microsc. Microanal. 10 (2004) 373. DOI:10.1017/S1431927604040565 PMid:15233856
[51] D.N. Seidman: Annu. Rev. Mater. Res. 37 (2007) 127. DOI:10.1146/annurev.matsci.37.052506.084200
[52] O.C. Hellman, J. Blatz du Rivage, D.N. Seidman: Ultramicrosc. 95 (2003) 199. DOI:10.1016/S0304-3991(02)00317-0
[53] O.C. Hellman, J.A. Vandenbroucke, J. Rüsing, D. Isheim, D.N. Seidman: Microsc. Microanal. 6 (2000) 437. PMid:11003678
[54] R.P. Kolli, D.N. Seidman: Microsc. Microanal. 13 (2007) 272. PMid:17637076; DOI:10.1017/S1431927607070675
[55] M.K. Miller, E.A. Kenik: Microsc. Microanal. 10 (2004) 336. PMid:15233851
[56] C.K. Sudbrack, D. Isheim, R.D. Noebe, N.S. Jacobson, D.N. Seidman: Microsc. Microanal. 10 (2004) 355. PMid:15233854; DOI:10.1017/S1431927604040589
[57] M.S. Gagliano, M.E. Fine: CALPHAD: Comput. Coupling Phase Diagrams Thermochem. 25 (2001) 207.
[58] M.S. Gagliano, M.E. Fine: Metall. Mater. Trans. A 35 (2004) 2323. DOI:10.1007/s11661-006-0212-x
[59] S.L. Meyer: Data analysis for Scientists and Engineers. New York: John Wiley & Sons, Inc. (1975).
[60] H.I. Aaronson, F.K. LeGoues: Metall. Trans. A 23 (1992) 1915. DOI:10.1007/BF02647541
[61] R. Wagner, R. Kampmann, P.W. Voorhees, in: G. Kosortz, editor. Phase Transformations in Materials. Weinheim, Germany: Wiley-VCH (2001) 309.
[62] C.J. Zener: J. Appl. Phys. 20 (1949)950. DOI:10.1063/1.1698258
[63] H.J. Jou, P.W. Voorhees, G.B. Olson: Computer simulations for the prediction of microstructure/property variation in aeroturbine disks, in: K.A. Green, T.M. Pollock, H. Harada, T.E. Howson, R.C. Reed, T.J. Schirra, S. Walston (Eds.) 10th International Symposium on Superalloys, TMS, Champion, PA (2004) 877.

(Received January 25, 2011; accepted July 29, 2011)

Bibliography

DOI 10.3139/146.110571
Int. J. Mat. Res. (formerly Z. Metallkd.)
102 (2011) 9; page 1115–1124

ISSN 1862-5282

Correspondence address

Dr. R. Prakash Kolli
E-mail: prakashkolli2007@u.northwestern.edu

Prof. Dr. David N. Seidman
Northwestern University
Department of Materials Science and Engeineering
2220 Campus Drive
Evanston, IL 60208-3108, USA
Tel.: +1 847 491 4391
Fax: +1 847 491 7820
E-mail: d.seidman@northwestern.edu

You will find the article and additional material by entering the document number **MK110571** on our website at *www.ijmr.de*